Energy 141 (2017) 1622–1628

Contents lists available at ScienceDirect

Energy

journal homepage: www.elsevier.com/locate/energy

Maximum recoverable gas from hydrate bearing sediments by depressurization

M. Terzariol [a, *], G. Goldsztein [b], J.C. Santamarina [a]

[a] Earth Science and Engineering, KAUST, Thuwal, 23955-6900, Saudi Arabia
[b] School of Mathematics, Georgia Institute of Technology, Atlanta, GA, 30332-0160, USA

ARTICLE INFO

Article history:
Received 5 November 2015
Received in revised form
1 November 2017
Accepted 12 November 2017
Available online 13 November 2017

Keywords:
Hydrates
Gas production
Methane
Sediments
Energy
Simulators

ABSTRACT

The estimation of gas production rates from hydrate bearing sediments requires complex numerical simulations. This manuscript presents a set of simple and robust analytical solutions to estimate the maximum depressurization-driven recoverable gas. These limiting-equilibrium solutions are established when the dissociation front reaches steady state conditions and ceases to expand further. Analytical solutions show the relevance of (1) relative permeabilities between the hydrate free sediment, the hydrate bearing sediment, and the aquitard layers, and (2) the extent of depressurization in terms of the fluid pressures at the well, at the phase boundary, and in the far field. Close form solutions for the size of the produced zone allow for expeditious financial analyses; results highlight the need for innovative production strategies in order to make hydrate accumulations an economically-viable energy resource. Horizontal directional drilling and multi-wellpoint seafloor dewatering installations may lead to advantageous production strategies in shallow seafloor reservoirs.

1. Introduction

Natural gas hydrates are crystalline water and gas compounds. Hydrate stability requires high fluid pressure and low temperature, as found in deep-water seafloor and lakebed sediments, and beneath the permafrost. Estimates of methane gas trapped in hydrate accumulations worldwide vary between 3×10^{15} m^3 and 10^{17} m^3, while the technically recoverable gas is estimated to be on the order of 3×10^{14} m^3 at standard temperature and pressure [1]. Table 1 summarizes the main characteristics of hydrate accumulations considered for gas extraction in Canada, China, India Japan, South Korea, and the USA. While gas can be produced by depressurization, thermal stimulation, inhibitor injection, and CO_2–CH_4 replacement, depressurization is preferred in most cases [17,18].

The analysis of gas production requires complex coupled thermo-hydro-chemo-mechanical simulators such as TOUGH+HYDRATE (original code: Pruess [19]; adaptation to hydrate studies: Moridis [20]; hydrate-specific simulator HydrateResSim reported in Hou et al. [21]), MH21-HYDRES [22], CMG-STARS (Computer Modelling Group; recent application in Sun et al. [23]), and STOMP-HYD [24], Code_Bright (original code: Olivella et al., [25]; adaptation to hydrate studies: Sanchez et al. [26]). These simulators involve multiple balance and conservation equations, depend on a large number of constitutive relations and parameters, and are challenged by time- and space-discretization constraints.

More tractable semi-analytical solutions have been proposed. Yet, analytical models for production evolution remain intricate (even in the simplest 1D model for production from hydrate-capped gas reservoirs by Tabatabaie and Pooladi-Darvish, [27]). In part, this complexity reflects the need to involve differential equations to capture time-dependent processes (e.g., the model for depressurization and thermal stimulation by Wang et al. [28]. As complexity increases, these analytical models require numerical solution (e.g., the model for depressurization and heating by Liu et el., [29]); eventually, they become hybrid-simulators (e.g., radial thermal dissociation by Omidi et al. [30].

The goal of this study is to predict the ultimate mass of gas that can be produced by depressurization from a single well. This analysis seeks to make the interaction among governing parameters self-evident in order to facilitate early economical scrutiny, without the need to model the evolution of production rate in time. The analysis is set when the dissociation front stops progressing as the fluid pressure reaches stability conditions away from the well. The ensuing analytical solutions provide the distance from the well

* Corresponding author.
E-mail address: marco.terzariol@kaust.edu.sa (M. Terzariol).

https://doi.org/10.1016/j.energy.2017.11.076
0360-5442/

Table 1
Characteristics of hydrate accumulations considered for gas extraction and estimated volumes of gas in place (at standard pressure and temperature). Note that the amounts of gas in place, technically recoverable gas and economically recoverable gas are frequently revised.

Location	Estimated Gas at STP [m^3]	Fluid Pressure u_{far} [MPa]	Intrinsic Permeability K	Initial Temperature T_o [K]	Sediment Porosity n	Hydrate Saturation S_{hyd}	Layer Thickness H [m]	Recovery Efficiency ε [7]
Mallik (Canada)	3×10^9 [1]	10 [1]	10^{-14} m^2 [1]	285 [1]	0.28 [1]	0.5 [1]	10–20 [1]	0.82–0.90
Gulf of Mexico (USA)	6×10^{14} [2]	20–30 [7]	1000 mD [8]	277–290 [7]	0.3–0.64 [8]	0.1–0.8 [8]	200 [8] (**)	0.65–0.93
Mount Elbert (Alaska, USA)	4×10^9 [2]	6 [9]	10^{-12} m^2 [9]	275 [9]	0.4 [9]	0.65 [9]	11 [9]	0.87–0.90
Blake Ridge (Atlantic, USA)	5×10^{12} [13]	30–35 [13]	ND	275–290 [7]	0.57 [13]	0–0.2 [13]	250 [13]	0.58–0.93
Hydrate Ridge (Pacific, USA)	2.3×10^{14} [2]	10–12 [7,12]	ND	285 [12]	0.6 [14]	0.3–0.4 [12]	10 [12]	0.79–0.82
Krishna-Godavari (India)	10^9 [6]	15 [6,7]	ND	279 [6]	0.6–0.7 [6]	0.04 [6]	180 [6]	0.79–0.90
Shenhu Area (China)	10^9 [5]	11 [10]	10^{-14} m^2 [10,15]	287 [10]	0.38 [10]	0.3 [10,15]	10 [10]	0.82–0.90
Ulleung Basin (South Korea)	10^{15}–10^{18} [3]	23 [3]	10^{-13} m^2 [3]	289 [3]	0.45–0.65 [3]	0.3–0.7 [3]	20 [3]	0.70–0.90
Nankai Trough (Japan)	5.6×10^{11} [4]	9–13 [11]	0.1–1000 mD [11]	287 [11]	0.3–0.4 [11]	0.1–0.95 [11]	70–100 [11]	0.70–0.93

References: [1] Moridis et al., [2]; [2] BOEM report [3]; [3] Moridis et al., [4]; [4] Fujii et al. [5]; [5] Wu et al. [6]; [6] Shankar and Riedel [7]; [7] recovery efficiency based on equations presented in Jang and Santamarina, [8]; [8] Myshakin et al. [9]; [9] Moridis et al. [10]; [10] Su et al. [11]; [11] Kurihara et al. [12]; [12] Trehu et al. [13]; [13] Collett and Ladd, [14]; [14] Suess et al. [15]; [15] Huang et al. [16]. Note: u_{far} = water pressure in the far field, K = intrinsic permeability of the sediment (units: as published), T_o = initial reservoir temperature, n = porosity, S_{hyd} = hydrate saturation, H = hydrate layer thickness; (**) Layers of 10 m over 200 m thick reservoir.

to the ultimate position of the dissociation front or "terminal radius" r*. This distance r* bounds the maximum amount of producible gas for a given well, and it defines the financial viability of gas extraction from hydrate bearing sediments. (Note: a similar analysis applies to thermal stimulation – See Li et al. [31] for a solution based on a moving Stefan boundary.)

1.1. Analytical solution

Consider a stable hydrate bearing sediment under high water pressure and low temperature. The reservoir is subjected to depressurization at the well. Gas production starts as soon as the pressure falls outside stability conditions. Eventually, steady state flow and pressure conditions are reached for a given well pressure u_w, the dissociation front stops advancing and hydrate dissociation ends. The distance from the well to the ultimate position of the dissociation boundary is the terminal radius r* and defines the size of the produced zone; the fluid pressure at r* is the pressure on the phase boundary u* for the reservoir temperature. This boundary defines two zones in the reservoir at the end of dissociation and under steady state flow conditions. The inner zone $r \leq r^*$ - that is characterized by the sediment permeability k_{sed} [m/s] (without hydrates but with partial water-gas saturation), the outer zone $r \geq r^*$ where hydrate bearing sediment has permeability k_{hbs} [m/s]. The water pressure in the far field is u_{far}.

Fig. 1 summarizes the boundary conditions for the three cases analyzed next: radial flow in a homogeneous formation or a strata-bound reservoir with either a vertical well normal to the reservoir or a horizontal well within it.

1.2. Total energy (flow) versus fluid pressure (hydrate stability)

The total energy E_{tot} field in the fluid around a production well governs flow patterns and it is defined by Laplace's equation $\nabla^2 E_{tot} = 0$ when mass conservation and Darcian conditions apply. The total energy E_{tot} at a point is a function of its elevation h_e from a reference datum and the fluid pressure u. On the other hand, hydrate stability conditions and the dissociation front are determined by the fluid pressure u. In most hydrate reservoirs the pressure change Δu needed to cause dissociation is much greater than the variation in elevation within the affected zone, $\Delta u \gg \Delta h_e \gamma_w$. Then, we can link total energy E_{tot} directly to fluid pressure u and rewrite Laplace's equation as $\nabla^2 u = 0$. Spherical, axisymmetric and 1D flow conditions are analyzed next by making use of this simplifying assumption.

1.3. Homogeneous formation: spherical radial flow

Radial flow. Laplace's equation in spherical coordinates is written as (sketch in Fig. 1a; Muskat [32]):

$$\nabla^2 u = \frac{1}{r^2}\frac{\partial}{\partial r}\left(r^2 \frac{\partial u}{\partial r}\right) + \frac{1}{r^2\, sin(\theta)}\frac{\partial}{\partial \theta}\left(sin(\theta)\, \frac{\partial u}{\partial \theta}\right) + \frac{1}{r^2\, sin^2(\theta)}\frac{\partial^2 u}{\partial \xi^2} = 0 \tag{1}$$

where the azimuthal angle θ, the polar angle ξ and the radius r define the location of any point in space. Tangential derivatives to equipotential lines vanish in radial flow, and the equation simplifies to:

$$\nabla^2 u = \frac{1}{r^2}\frac{\partial}{\partial r}\left(r^2 \frac{\partial u}{\partial r}\right) = 0 \tag{2}$$

The general form of the solution is:

$$u_r = a - \frac{b}{r} \tag{3}$$

where a and b are constants. If fluid pressures u_1 and u_2 are known at radial distances r_1 and r_2, then the pressure field u_r is:

$$u_r = u_1 + (u_2 - u_1)\left(\frac{r_1 - r}{r_1 - r_2}\right)\frac{r_2}{r} \tag{4}$$

The flow rate q [m^3/s] can be computed from the flux across a sphere of area $4\pi r^2$ when the Darcy velocity is $(k/\gamma)\, \partial u/\partial r$:

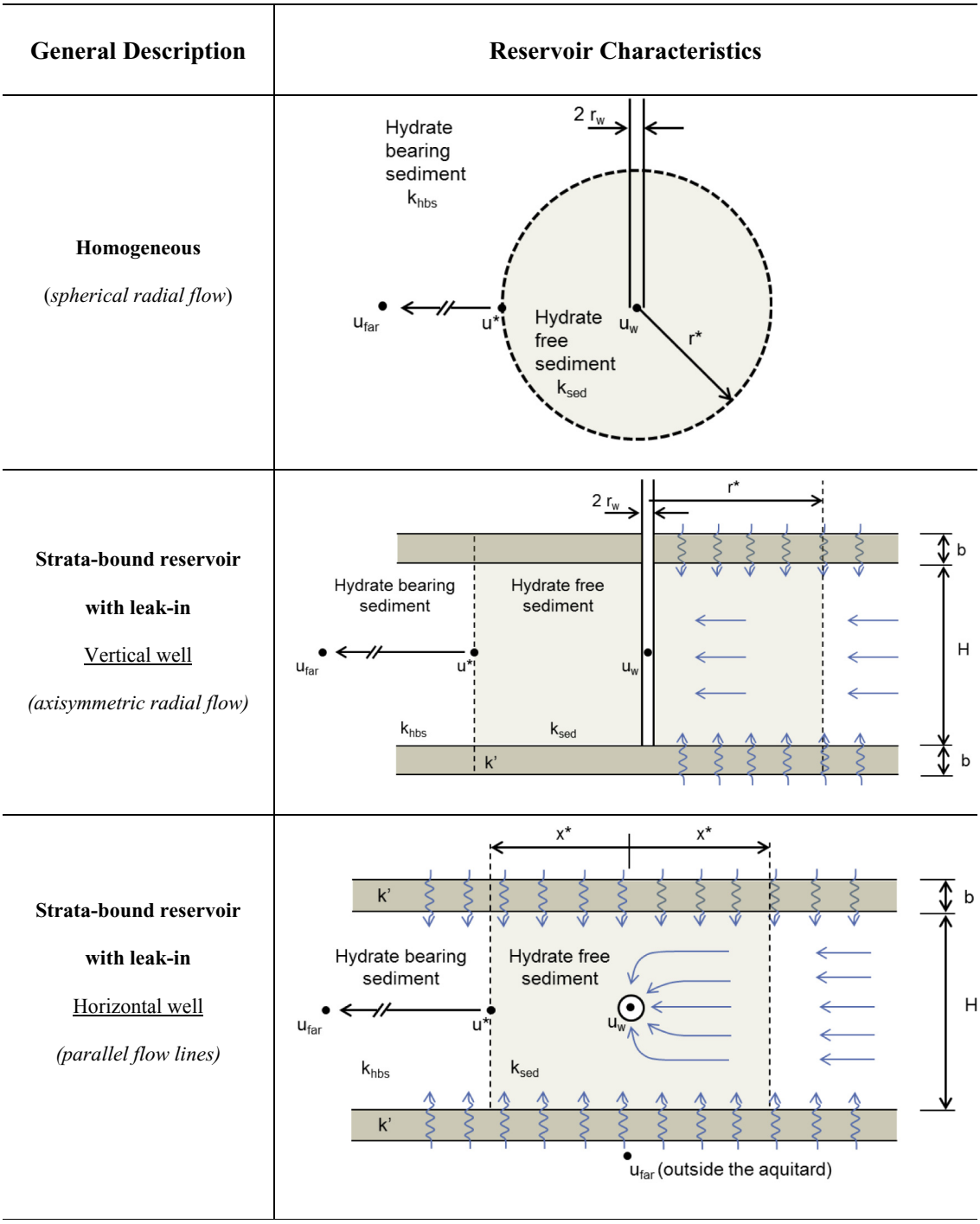

Fig. 1. Reservoir characteristics and flow conditions. Well radius r_w in hydrate bearing sediment layer thickness H and permeability k_{hyd} before dissociation and k_{sed} after dissociation. Aquitard permeability k' and thickness b. Fluid pressure at the well u_w, at the phase boundary u^* and in the far field u_{far}. Terminal size of the dissociation front in radial r^* or parallel x^* flow.

$$q = -4\,\pi\,r^2 \frac{k}{\gamma_w}\frac{\partial u_r}{\partial r} = 4\,\pi \frac{k}{\gamma_w}\frac{(u_2-u_1)}{\frac{1}{r_1}-\frac{1}{r_2}} \quad (5)$$

Dissociation Boundary Terminal Radius r.* When the dissociation front stops expanding at the terminal radius r^*, mass conservation implies that the water flow rate is constant across the boundary r^* between the inner hydrate-free sediment q_{sed} (sub-index 'sed' for sediment) and outer hydrate bearing sediment q_{hbs} (sub-index 'hbs' for hydrate bearing sediment):

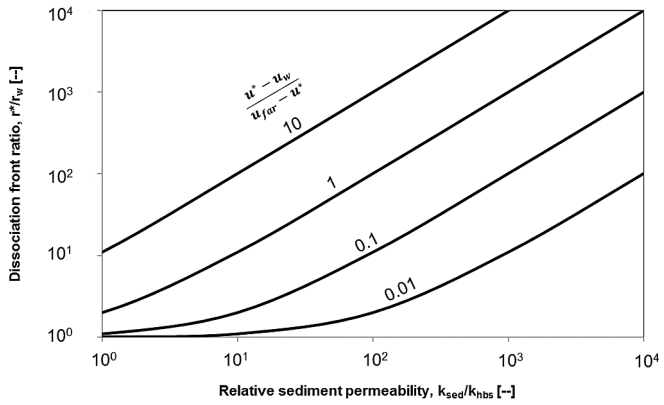

Fig. 2. Spherical dissociation front in homogeneous medium under radial flow. Relationship between the terminal dissociation radius normalized by the well size r^*/r_w as a function of the relative permeability between the hydrate-free and hydrate-bearing sediment k_{sed}/k_{hyd}. Trends shown for different relative depressurization values $(u^*-u_w)/(u_{far}-u^*)$ where u_w = well water pressure, u^* = dissociation pressure, and u_{far} = far field water pressure.

$$q_{sed} = q_{hbs} \quad \text{at } r = r^* \textit{ under steady state} \tag{6}$$

From Equation (5),

$$\frac{(u^* - u_w)k_{sed}}{\frac{1}{r_w} - \frac{1}{r^*}} = \frac{\left(u_{far} - u^*\right)k_{hbs}}{\frac{1}{r^*} - \frac{1}{r_{far}}} \tag{7}$$

Then, the terminal radius of the dissociation front r^* can be recovered from Equation (7) (Note: $r_{far} \gg r^*$ - Fig. 2):

$$r^* = r_w\left(1 + \frac{k_{sed}}{k_{hbs}}\,\frac{u^* - u_w}{u_{far} - u^*}\right) \tag{8}$$

The three water pressures involved in Equations (7) and (8) are: the dissociation pressure u^* (on the phase boundary), the production pressure imposed at the well u_w, and the water pressure in the far field u_{far} (Note: these pressures are selected at the elevation of the well to minimize the effect of deviations from the original assumption, $\Delta u \gg \Delta h_e\,\gamma_w$). This expression captures the interplay between pressures (u^*, u_w, u_{far}) and permeabilities (k_{sed}, k_{hbs}) in defining the production zone size r^* relative to the effective well size r_w.

1.4. Strata-bound reservoir with leak-in: well normal to the reservoir

General solution. Consider a layered stratigraphy with a hydrate bearing layer of thickness H confined between two low-permeability layers of thickness b and permeability k' [m/s] (Fig. 1b). Continuity must take into consideration the contribution of radial flow plus the transverse flow "leaking-in" from upper and lower layers. Then, mass conservation across an annular ring surrounding the well at radial distance r with leak-in across its thickness dr requires:

$$\frac{\partial^2 \overline{\overline{u}}}{\partial r^2} + \frac{1}{r}\,\frac{\partial \overline{\overline{u}}}{\partial r} - \frac{\overline{\overline{u}}}{\lambda^2} = 0 \tag{9}$$

where $\overline{\overline{u}} = u_r - u_{far}$, and $\lambda = \sqrt{\frac{k\,H\,b}{2\,k'}}$. The axisymmetric pressure field u_r that satisfies Equation (9) is:

$$u_r = u_{far} + A\,I_o\left(\frac{r}{\lambda}\right) + B\,K_o\left(\frac{r}{\lambda}\right) \tag{10}$$

This equation is solved for the inner hydrate-free zone (boundary conditions: $u = u_w$ at $r = r_w$ and $u = u^*$ at $r = r^*$) and the outer boundary hydrate bearing zone (boundary conditions: $u = u^*$ at $r = r^*$, and $u = u_{far}$ at $r = r_{far}$).

The flow rate q [m^3/s] in each zone is the integral of the flux across a cylindrical surface area $2\pi rH$ with Darcy velocity $(k/\gamma)\,\partial u/\partial r$. In particular, the flow rate for the inner zone ($r_w \le r \le r^*$) is:

$$\begin{aligned} q_{sed} &= -2\,\pi\,r\,H\,\frac{k_{sed}}{\gamma_w}\,\frac{\partial u_r}{\partial r} \\ &= \frac{2\,\pi\,r\,H}{\lambda_{sed}}\,\frac{k_{sed}}{\gamma_w}\left[B_{sed}\,K_1\left(\frac{r}{\lambda_{sed}}\right) - A_{sed}\,I_1\left(\frac{r}{\lambda_{sed}}\right)\right] \end{aligned} \tag{11}$$

where K_1 is the modified hyperbolic Bessel function of the second kind and order one, I_1 is the modified hyperbolic Bessel function of the first kind and order one, the characteristic length is $\lambda_{sed} = \sqrt{\frac{k_{sed}\,H\,b}{2\,k'}}$, and A_{sed} and B_{sed} are constants defined as:

$$A_{sed} = \frac{u^* - u_{far}}{I_o\left(\frac{r^*}{\lambda_{sed}}\right)} - \frac{B\,K_o\left(\frac{r^*}{\lambda_{sed}}\right)}{I_o\left(\frac{r^*}{\lambda_{sed}}\right)} \tag{12}$$

$$B_{sed} = \frac{u_w - u_{far} - \left(u^* - u_{far}\right)\frac{I_o\left(\frac{r_w}{\lambda_{sed}}\right)}{I_o\left(\frac{r^*}{\lambda_{sed}}\right)}}{K_o\left(\frac{r_w}{\lambda_{sed}}\right) - K_o\left(\frac{r^*}{\lambda_{sed}}\right)\frac{I_o\left(\frac{r_w}{\lambda_{sed}}\right)}{I_o\left(\frac{r^*}{\lambda_{sed}}\right)}} \tag{13}$$

where K_0 is the modified hyperbolic Bessel function of the second kind and order zero and I_0 is the modified hyperbolic Bessel function of the first kind and order zero.

On the other hand, the axisymmetric pressure field for the outer zone (Equation (10) $r \ge r^*$) reduces to:

$$u_r = u_{far} - \left(u^* - u_{far}\right)\frac{K_o\left(\frac{r}{\lambda}\right)}{K_o\left(\frac{r^*}{\lambda}\right)} \tag{14}$$

and, the flow rate for the outer zone becomes ($r \ge r^*$):

$$\begin{aligned} q_{hbs} &= -\,2\,\pi\,r\,H\,\frac{k_{hbs}}{\gamma_w}\,\frac{\partial u_r}{\partial r} \\ &= \frac{2\,\pi\,r\,H}{\lambda_{hbs}}\,\frac{k_{hbs}}{\gamma_w}\left(u^* - u_{far}\right)\frac{K_1\left(\frac{r}{\lambda_{hbs}}\right)}{K_o\left(\frac{r^*}{\lambda_{hbs}}\right)} \end{aligned} \tag{15}$$

where the characteristic length is $\lambda_{hbs} = \sqrt{\frac{k_{hbs}\,H\,b}{2\,k'}}$.

Dissociation Boundary Terminal Radius r^*. Once again, the water flow rate across the boundary at $r = r^*$ under steady state conditions must be the same $q_{sed} = q_{hbs}$ (Equation (6)). Therefore, combining Equations (11) and (15),

$$\left[B_{sed}\,K_1\left(\frac{r^*}{\lambda_{sed}}\right) - A_{sed}\,I_1\left(\frac{r^*}{\lambda_{sed}}\right)\right] = \left(u^* - u_{far}\right)\sqrt{\frac{k_{hbs}}{k_{sed}}}\,\frac{K_1\left(\frac{r^*}{\lambda_{hbs}}\right)}{K_o\left(\frac{r^*}{\lambda_{hbs}}\right)} \tag{16}$$

The size of the production zone is the value of r^* that satisfies this equality. As in the previous case, this solution explicitly captures the effects of relative permeabilities between the seal layers and the formation before and after dissociation (Note: the effect of

permeability in layer-bound reservoirs is implicitly explored in a recent numerical study by Chen et al. [33]).

1.5. Strata-bound reservoir with leak-in: horizontal well embedded in the reservoir

General Solution. The layered formation is the same as in the previous case but the well has been drilled parallel to the layers along the center of the reservoir for a length L » H (Fig. 1c). Mass conservation across a slice of the reservoir of thickness dx with leak-in from upper and lower aquitards results in:

$$\frac{\partial^2 \overline{\overline{u}}}{\partial x^2} - \frac{\overline{\overline{u}}}{\lambda^2} = 0 \tag{17}$$

where $\overline{\overline{u}} = 0 = u_x - u_{far}$, and the characteristic length is $\lambda = \sqrt{\frac{k\,H\,b}{2\,k'}}$. The pressure field u_x that satisfies Equation (17) is

$$u_x = u_{far} + A\,e^{\left(\frac{x}{\lambda}\right)} + B\,e^{\left(-\frac{x}{\lambda}\right)} \tag{18}$$

where A and B are constant. As in previous cases, this equation is solved for the inner hydrate-free zone (with λ_{sed} in terms of $k = k_{sed}$) and the outer boundary hydrate bearing zone (with λ_{hbs} in terms of $k = k_{hbs}$).

The Darcian flow rate q_{sed} in the inner zone is (inner zone $x \le x^*$, but at a distance x such that $r_w \ll x \le x^*$ to avoid local radial flow effects near the well)

$$\begin{aligned} q_{sed} &= -2\,L\,H\frac{k_{sed}}{\gamma_w}\frac{\partial u_x}{\partial x} \\ &= \frac{2\,L\,H}{\lambda_{sed}}\frac{k_{sed}}{\gamma_w}\left[A_{sed}\,e^{\left(\frac{x}{\lambda_{sed}}\right)} - B_{sed}\,e^{\left(-\frac{x}{\lambda_{sed}}\right)}\right] \end{aligned} \tag{19}$$

and the constants A_{sed} and B_{sed} are:

$$A_{sed} = -u_{far}\left[2 + e^{\left(\frac{x^*}{\lambda_{sed}}\right)}\right] - u^* - u_w\left[e^{\left(\frac{x^*}{\lambda_{sed}}\right)} - 1\right] \tag{20}$$

$$B_{sed} = u^* - u_{far} - \left(u_w - u_{far}\right)e^{\left(\frac{x^*}{\lambda_{sed}}\right)} \tag{21}$$

For the outer zone, Equation (18) simplifies to ($x > x^*$)

$$u_x = u_{far} - \left(u^* - u_{far}\right)e^{\left(\frac{x^* - x}{\lambda_{hbs}}\right)} \tag{22}$$

and the flow rate q_{hbs} in the outer zone becomes ($x > x^*$):

$$\begin{aligned} q_{hbs} &= -2\,L\,H\,\frac{k_{hbs}}{\gamma_w}\frac{\partial u_x}{\partial x} \\ &= \frac{2\,L\,H}{\lambda_{hbs}}\,\frac{k_{hbs}}{\gamma_w}\left(u_{far} - u^*\right)e^{\left(\frac{x^* - x}{\lambda_{hbs}}\right)} \end{aligned} \tag{23}$$

Dissociation Boundary Terminal Size x.* The water flow rate in the inner and outer zones must be equal $q_{sed} = q_{hbs}$ when $x = x^*$. Then, Equations (19) and (23) predict:

$$\left[\frac{2\,u_{far}}{\left(u_{far} - u^*\right)}\,e^{\left(\frac{x^*}{\lambda_{sed}}\right)} + \frac{\left(u_{far} - u_w\right)}{\left(u_{far} - u^*\right)}\left(e^{\left(\frac{x^*}{\lambda_{sed}}\right)} - e^{\left(\frac{2x^*}{\lambda_{sed}}\right)}\right) - 2\cosh\left(x^*\right)\right] = \sqrt{\frac{k_{hbs}}{k_{sed}}} \tag{24}$$

The terminal position of the dissociation front is the value of x^* that satisfies Equation (24).

2. Discussion

Governing dimensionless ratios - Trends. Solutions for spherical, and layer-bound flow anticipate that the size of the production zone increases (Equations (8), (16) and (24); refer to Fig. 2 for the simpler spherical case): (1) when the initial pressure is close to the phase boundary (u_{far}–u^*)→0, (2) when high depressurization is imposed at the well, i.e., large u_{far}–u_w (in agreement with experimental evidence in Yang et al. [34], (3) in sediments with high hydrate saturation k_{sed}/k_{hbs} »1 (see permeability effects in Zhao et al. [35]), (4) in tight aquitard layers k_{sed}/k'»1, and (5) in thick reservoirs bound between thick aquitard layers, $H{\cdot}b/r_w^2$»1.

Effective well size. Spherical and axisymmetric cases show a proportionality between the size of the production zone r^* and the effective well size r_w (Fig. 2 – Note: the effect of well size is absent in the solution far from the well x^* » r_w adopted for the strata-bound well embedded in the reservoir). Therefore, well completions that involve enlarged sand packs around the screen extend the production zone r^*. We consider that r_w is the size of the highly pervious zone around the well where the fluid pressure remains relatively constant $u \approx u_w$.

Comparison with numerical simulators. The analysis conducted here is for steady-state conditions at the end of gas production. Fig. 3 compares published production zones r^* estimated from numerical simulations run until quasi-stable conditions and terminal radius r^* values obtained using the proposed analytical

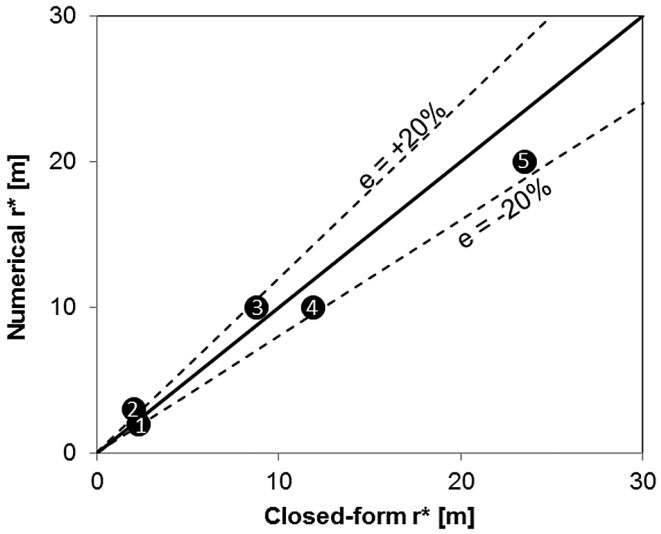

Fig. 3. Terminal size of the dissociation front computed using numerical simulators (values recovered from the literature) and estimated values using the closed-form solution for the strata-bound reservoir with leak-in conditions when the well is normal-the reservoir. Cases: (1) Mallik, Canada [2]; (2) Shenhu, China [11]; (3) Hypothetical case [22]; (4) Hypothetical case [36]; (5) Mt. Elbert, Alaska [37].

solutions for layered stratigraphy with normal well (Equation (16)). Numerical values are in good agreement with analytical predictions for layered stratigraphy; deviations reflect differences in boundary conditions and incomplete simulation time for long-term steady state at the end of dissociation. A targeted evaluation based on the Code-BRIGHT simulator shows full agreement with the analytical solution (Case: well normal to strata-bound reservoir with leak-in – Sanchez (2017), Personal communication).

Field conditions. Evolving field conditions are complex as the decrease in pore water pressure causes an increase in the sediment effective stress; hence, the sediment compacts and its permeability k_{sed} decreases. Analyses using the close form solutions presented here should consider ultimate sediment parameters k_{sed} and k'.

Embodied Energy - Economics. The embodied energy EE [J] in recoverable gas is computed from the energy density of methane gas $E_d = 46$ MJ/kg, or of hydrate $E_d = 4.8$ MJ/kg [38]. For a hydrate bearing sediment with porosity n and hydrate saturation S_{hyd}, the embodied energy in a producible volume V is:

$$EE = \varepsilon \; n \; S_{hyd} \; V \; E_d \; \rho_{hyd} \tag{25}$$

where the producible volume is a function of the size of the produced zone, either r* for spherical (Equation (8)) and axisymmetric geometries (Equation (16)), or x* for the case of the well embedded in the layered reservoir (Equation (24)). The recovery efficiency ε depends on capillary effects in the sediment and it is a function of pore size distribution and connectivity. The maximum gas recovery efficiency is:

$$\varepsilon = \frac{\beta - 1}{\beta - 0.79} \tag{26}$$

where the fluid expansion factor β depends on the extent of depressurization [8]. Values for reservoirs listed in Table 1 range between $\beta = 1.3$ and $\beta = 4$, which corresponds to efficiencies between $\varepsilon = 0.58$ and $\varepsilon = 0.93$ respectively. Finally, the monetary value of a well MV [$] combines the embodied energy EE and the price of energy PE [$/J], MV = PE·EE, and it should outweigh the installation/production cost, PC [$/well].

Let's consider an advantageous case for production. It consists of a $H = 5$ m thick reservoir, at an initial fluid pressure $u_{far} = 12$ MPa and a temperature such that the pressure on the phase boundary is $u^* = 8$ MPa. The reservoir is bound by two $b = 1$ m thick aquitards. The effective well size is assumed to be $r_w = 0.5$ m (see discussion on effective well size above) so that the geometric ratio is $H \cdot b/r_w^{2=}$ 20. Hydraulic conductivities in the hydrate-free sediment k_{sed}, hydrate bearing sediment k_{hbs} and aquitard k' result in relative ratios $k_{hbs}/k' = 10^2$ and $k_{sed}/k_{hbs} = 10^2$. The fluid pressure at the well is lowered to $u_w = 4$ MPa. Then, the ultimate size of the production zone is $r^* = 85$ m (Equation (16)). If the reservoir has a porosity $n = 0.35$, and a degree of hydrate saturation $S_{hyd} = 0.7$, the total embodied energy will be $EE = 10^8$ MJ (assumes energy density of hydrate $E_d = 4.8$ MJ/k; hydrate mass density $\rho_{hyd} = 920$ kg/m^3; the gas recovery efficiency computed for the target depressurization pressure is $\varepsilon = 0.83$). Drilling and operation costs would have to be PC = 100,000 US$ per well to break even in a market situation where the price of energy is PE = 0.008 US$/MJ (based on an oil price ~50 $/bbl). This result highlights the need for innovative production strategies in order to make hydrate accumulations an economically viable energy resource.

Production strategy. Fig. 4 shows a comparison of geometric effects for the same reservoir characteristics used for the previous example. The well pressure u_w is varied from 0 to 8 MPa. The advantage of a directional well drilled along the reservoir is evident: the produced zone is more than twice wider than in the case of a well normal to the reservoir ($x^* = 2.2\, r^*$), and the produced volume scales linearly with the length of the well along the reservoir L.

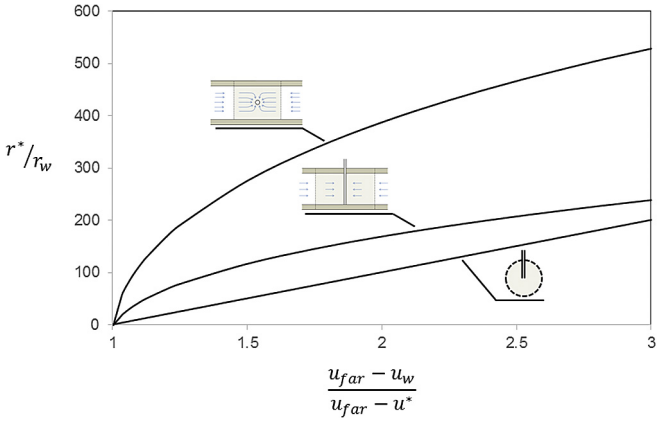

Fig. 4. Terminal size of the produced zone for the reservoir geometries and flow conditions analyzed here (Refer-Fig. 1). For a given depressurization, the horizontal well embedded in the reservoir will lead to a larger production zone, i.e., x*>r*. In this example, the horizontal well can cause dissociation to a distance 2.2 times larger than a well normal the reservoir. Parameters used for these simulations: $k_{hbs}/k' = 10^2$, $H \cdot b/r_w^{2=}$ 20, $k_{sed}/k_{hbs} = 100$, $H = 5$ m and $r_w = 0.5$ m; $u_{far} = 12$ MPa and $u^* = 8$ MPa. The well pressure varies from 0 to 8 MPa.
Maximum Recoverable Gas from Hydrate Bearing Sediments by Depressurization.

Shallow seafloor reservoirs. Directional wells may be drilled into shallow seafloor reservoirs by adapting on-shore "horizontal directional drilling" HDD technology developed for urban utilities. Alternatively, a multi-wellpoint seafloor dewatering installation may prove effective for shallow accumulations (see experiments in Wang et al., [28]).

3. Conclusions

During depressurization, the dissociation front advances away from the well until it reaches a terminal radius/distance where the fluid pressure is back inside the stability field (Note: a similar observation applies to thermally driven dissociation). The analysis of steady state flow at the terminal condition avoids the complex analysis of coupled processes involved in production rate studies.

Solutions for the terminal radius/distance presented in this manuscript apply to disseminated pore-filling hydrates (i.e., sandy sediments) in either homogeneous reservoirs with spherical radial flow or layered reservoir with strata-bound flow.

Analytical solutions explicitly show the interplay between dimensionless ratios defined by (1) the terminal radius/distance and the effective well diameter or strata-bound reservoir geometry, (2) the relative permeabilities of the sediment with and without hydrates and the permeability of the seal layer, and (3) the extent of depressurization at the well relative to the pressure at the phase boundary and in the far field.

Mathematical solutions clearly show that the size of the production zone or terminal radius/distance increases when the in situ fluid pressure is close to the phase boundary, when high depressurization is imposed at the well, in sediments with high hydrate saturation, in tight aquitard layers, and in thick reservoirs bound between thick aquitard layers. The dissociation distance increases when wells are drilled along the reservoir horizon; then, the affected volume is proportional to the length of the well in the formation.

Close form solutions for the terminal radius/distance allow for expeditious cost-analyses. Results highlight the need for innovative production strategies in order to make hydrate accumulations an

economically viable energy resource. Horizontal directional drilling and multi-wellpoint seafloor dewatering installations may lead to economically viable production strategies in shallow coarse-grained seafloor reservoirs.

Acknowledgements

Support for this research was provided by the USA Department of Energy, DE-FC26-06NT42963, with additional funding by the KAUST endowment. G. E Abelskamp edited this manuscript.

References

[1] Boswell R, Collett TS. Current perspectives on gas hydrate resources. Energy Environ Sci 2011;4(4):1206–15.
[2] Moridis GJ, Collett TS, Dallimore SR, Satoh T, Hancock S, Weatherhill B. Numerical simulation studies of gas production scenarios from hydrate accumulations at the Mallik Site, McKenzie Delta, Canada. In: 4th Int.Conf. Gas hydrates; 2002. p. 239–44.
[3] Bureau of Ocean Energy and Management -BOEM. Assessment of in-place gas hydrate resources of the lower 48 United States outer continental shelf. BOEM; 2012. p. 4.
[4] Moridis GJ, Kim J, Reagan MT, Kim S-J. Feasibility of gas production from a gas hydrate accumulation at the UBGH2-6 site of the Ulleung basin in the Korean East Sea. J Pet Sci Eng 2013;108:180–210.
[5] Fujii T, Noguchi S, Takayama T, Suzuki K, Yamamoto K, Saeki T. Site selection and formation evaluation at the 1st offshore methane hydrate production test site in the Eastern Nankai trough, Japan. In: Proc., 75th EAGE conference & exhibition-workshops, london; 2013.
[6] Wu N, Yang S, Zhang H, Liang J, Wang H, Lu Ja. Gas hydrate System of Shenhu area northern South China Sea: wire-line logging geochemical results and preliminary resources estimates. In: Paper 20485. Proc., offshore technology conference; 2010.
[7] Shankar U, Riedel M. Gas hydrate saturation in the Krishna-Godavari basin from P-wave velocity resistivity logs. Mar Pet Geol 2011;28:1768–78.
[8] Jang J, Santamarina JC. Recoverable gas from hydrate-bearing sediments: pore network model simulation and macroscale analyses. J Geophys Res Solid Earth 2011;116(B8).
[9] Myshakin EM, Gaddipati M, Rose K, Anderson BJ. Numerical simulations of depressurization-induced gas production from gas hydrate reservoirs at the Walker Ridge 313 site, northern Gulf of Mexico. Mar Pet Geol 2012;34(1):169–85.
[10] Moridis GJ, Collett T, Pooladi-Darvish M, Hancock S, Santamarina JC, Boswell R, et al. Challenges, uncertainties and issues facing gas production from gas hydrate deposits. SPE Reserv Eval Eng 2011;14(1):76–112.
[11] Su Z, He Y, Wu N, Zhang K, Moridis GJ. Evaluation on gas production potential from laminar hydrate deposits in Shenhu Area of South China Sea through depressurization using vertical wells. J Pet Sci Eng 2012;86:87–98.
[12] Kurihara M, Sato A, Ouchi H, Narita H, Masuda Y, Saeki T, et al. Prediction of gas productivity from Eastern Nankai Trough methane-hydrate reservoirs. SPE Reserv Eval Eng 2009;12(03):477–99.
[13] Trehu AM, Long PE, Torres ME, Bohrmann G, Rack FR, Collett TS, et al. Three-dimensional distribution of gas hydrate beneath southern Hydrate Ridge: constraints from ODP Leg 204. Earth Planet Sci Lett 2004;222:845–62.
[14] Collett TS, Ladd J. Detection of gas hydrate with downhole logs and assessment of gas hydrate concentrations (saturations) and gas volumes on the Blake Ridge with electrical resistivity log data. Proc Ocean Drill Program 2000;164.
[15] Suess E, Torres ME, Bohrmann G, Collier RW, Rickert D, Goldfinger C, et al. Sea floor methane hydrates at hydrate ridge, cascadia margin. Geophys Monogr Am Geophys Union 2001;124:87–98.
[16] Huang L, Su Z, Wu N-Y. Evaluation on the gas production potential of different lithological hydrate accumulations in marine environment. Energy 2015;91:782–98.
[17] Bhade P, Phirani J. Gas production from layered methane hydrate reservoirs. Energy 2015;82:686–96.
[18] Reagan MT, Moridis GJ, Johnson JN, Pan L, Freeman CM, Pan L, et al. Field-Scale simulation of production from oceanic gas hydrate deposits. Transp Porous Media 2015;108:151–69.
[19] Pruess K. The TOUGH codes—a family of simulation tools for multiphase flow and transport processes in permeable media. Vadose Zone J 2004;3(3):738–46.
[20] Moridis GJ. TOUGH+ HYDRATE v1. 2 User's manual: a code for the simulation of system behavior in hydrate-bearing geologic media. R. LBNL-3185, ed. Berkeley, CA: Lawrence Berkeley National Laboratory; 2014.
[21] Hou J, Xia Z, Li S, Zhou K, Lu N. Operation parameter optimization of a gas hydrate reservoir developed by cyclic hot water stimulation with a separated-zone horizontal well based on particle swarm algorithm. Energy 2016;96:581–91.
[22] Konno Y, Masuda Y, Hariguchi Y, Kurihara M, Ouchi H. Key factors for depressurization-induced gas production from oceanic methane hydrates. Energy & Fuels 2010;24(3):1736–44.
[23] Sun Z, Xin Y, Sun Q, Ma R, Zhang J, Lv S, et al. Numerical simulation of the depressurization process of a natural gas hydrate reservoir: an attempt at optimization of field operational factors with multiple wells in a real 3D geological model. Energies 2016;9.
[24] White MD, McGrail BP. STOMP-HYD: a new numerical simulator for analysis of methane hydrate production from geologic formations. In: Proceedings of 2nd international symposium on gas hydrate technology; 2006.
[25] Olivella S, Gens A, Carrera J, Alonso EE. Numerical formulation for a simulator (CODE - BRIGHT) for the coupled analysis of saline media. Eng Comput 1996;13:87–112.
[26] Sanchez M, Gai M, Santamarina JC. A constitutive mechanical model for gas hydrate bearing sediments incorporating inelastic mechanisms. Comput Geotech 2017;84:28–46.
[27] Tabatabaie SH, Pooladi-Darvish M. Analytical solution for gas production from hydrate reservoirs underlain with free gas. J Nat Gas Sci Eng 2009;1:46–57.
[28] Wang Y, Feng J-C, Li X-S, Zhang Y, Li G. Analytic modeling and large-scale experimental study of mass and heat transfer during hydrate dissociation in sediment with different dissociation methods. Energy 2015;90:1931–48.
[29] Liu L, Lu X, Zhang X. A theoretical model for predicting the spatial distribution of gas hydrate dissociation under the combination of depressurization and heating without the discontinuous interface assumption. J Pet Sci Eng 2015;133:589–601.
[30] Omidi M, Shahsavand A, Mohammadi HS. Modeling and simulation of hydrate thermal dissociation around gas production pipe from suboceanic sediment. J Nat Gas Sci Eng 2016;32:48–58.
[31] Li M, Fan S, Su Y, Ezekiel J, Lu M, Zhang L. Mathematical models of the heat-water dissociation of natural gas hydrates considering a moving Stefan boundary. Energy 2015;90:202–7.
[32] Muskat M. Flow of homogeneous fluids. JW Edwards. Ann Arbor, Michigan: J.W. Edwards Inc.; 1965.
[33] Chen L, Feng Y, Kogawa T, Okajima J, Komiya A, Maruyama S. Construction and simulation of reservoir scale layered model for production and utilization of methane hydrate: the case of Nankai Trough Japan. Energy 2017;143:128–40. ISSN 0360-5442.
[34] Yang M, Fu Z, Jiang L, Song Y. Gas recovery from depressurized methane hydrate deposits with different water saturations. Appl Energy 2017;187:180–8.
[35] Zhao J, Fan Z, Dong H, Yang Z, Song Y. Influence of reservoir permeability on methane hydrate dissociation by depressurization. Int J Heat Mass Transf 2016;103:265–76.
[36] Moridis GJ, Kowalsky MB, Pruess K. Depressurization-induced gas production from class-1 hydrate deposits. SPE Reserv Eval Eng 2007;10(5):458–81.
[37] Moridis GJ, Silpngarmlert S, Reagan MT, Collett T, Zhang K. Gas production from a cold, stratigraphically-bounded gas hydrate deposit at the mount Elbert gas hydrate stratigraphic test well, Alaska North slope: implications of uncertainties. Mar Pet Geol 2011;28(2):517–34.
[38] Hermann WA. Quantifying global exergy resources. Energy 2006;31(12):1685–702.